applied sciences

MDPI

Article

Cooperative Control of Interconnected Air Suspension Based on Model Predictive Control

Ying Zhou [1], Zhongxing Li [1,*], Wenhao Yu [2] and Yi Yu [1]

[1] School of Automotive and Traffic Engineering, Jiangsu University, Zhenjiang 212013, China
[2] School of Vehicle and Mobility, Tsinghua University, Beijing 100084, China
* Correspondence: zhxli@ujs.edu.cn

Abstract: The suspension system is a significant part of a vehicle because it transmits the torque and force between the wheels and the frame, meeting the requirements of ride comfort. In this paper, a novel interconnected air suspension was introduced and a cooperative control between interconnected mode activation (IMA) and outsourced mode activation (OMA) was designed. To improve ride comfort in a bus at a minimal energy consumption, this cooperative control based on model predictive control (MPC) for computing the best force and the rule was defined to distribute the best suspension force generated by IMA and OMA. The simulation and experimental results showed that the proposed control strategy significantly improved ride comfort in different conditions. Compared with traditional control in the test vehicle, the RMS of the front-left sprung mass and unsprung vertical acceleration decreased by 24.2% and 14.5%, respectively, under a straight condition; the RMS of the sprung (unsprung) mass vertical acceleration reduced by 22.38% and 15.43%, respectively, under a bump condition.

Keywords: interconnected air suspension; model predictive control; cooperative control; ride comfort; interconnected mode

Citation: Zhou, Y.; Li, Z.; Yu, W.; Yu, Y. Cooperative Control of Interconnected Air Suspension Based on Model Predictive Control. *Appl. Sci.* **2022**, *12*, 9886. https://doi.org/10.3390/app12199886

Academic Editor: Rosario Pecora

Received: 28 August 2022
Accepted: 26 September 2022
Published: 30 September 2022

1. Introduction

The suspension system is the transmission device connecting the wheels and the body, and mainly undertakes the sprung mass and ensures good contact between the tires and the road, as well as reducing uneven excitation from the road surface [1,2]. Air suspension is a typical semi-active suspension, which has the characteristics of variable stiffness and low vibration frequency, which can effectively improve vehicle handling and ride comfort [3]. Researchers have studied roll [4], pitch [5], elimination torsion [6], and stability [7] in the air suspension field. Moreover, air suspension consumes less energy than active suspension. Air suspension is considered to have broad application prospects [8].

Interconnected air suspension (IAS) is developed by using pipes to connect the air springs in a suspension system. There is an excellent performance in vibration isolation and adjusting the pitch and roll stiffness by switching the interconnected modes of the IAS. To improve vehicle performance, some scholars carried out several control strategies in ISA and received good results. Sun et al. [9] proposed a cooperative control strategy based on interconnection state logic switching and game control of distributed damping. The result showed that this coordinated system can significantly improve ride comfort and restrain the pitching motion. Hossein Nazemian et al. [10] developed an optimized hybrid fuzzy-PID to control the height and roll angle in a novel interconnected air suspension system. The result showed that the roll angle is improved compared with a passive case and conventional configuration. Kai Cao et al. [11] designed a PID transverse interconnected electronic control air suspension system controller based on a seeker optimization algorithm. The research result showed that the proposed control strategy effectively improved ride comfort and operation stability of the vehicle. However, there is little research on the cooperative control of outsourced mode activation (OMA) and interconnected mode activation (IMA).

It is difficult to define an effective rule to avoid charging and discharging gas at the same in one spring when the OMA and IMA work at the same time.

Compared with the above control strategies, MPC has advantages against the limitation from the process dead-time, nonminimum phase, and process dynamic due to the predictions over the future horizon [12]. When it comes to activation saturation control problems, MPC allows explicit taking into account of the effect of input and state constraints in the control design step [13]. MPC has been successfully implemented on a large number of industrial processes [14,15]. Some scholars designed an MPC approach for semi-active suspension systems. Nguyen et al. [16] proposed MPC, which gave a trade-off between ride comfort and road holding while guaranteeing physical constraints of the semi-active dampers in the suspension system. Simulation results showed the effectiveness of the proposed approach. Hu et al. [17] multiplexed an MPC controller integrated with soft constraints, and a Kalman filter is proposed based on a full-car model. The results show that the overall performance of ride comfort and roadholding could be improved significantly. Yang et al. [18] presented MPC of a new semiactive hydro-pneumatic inerter-based suspension system. The results of the numerical simulations and experiments verify the effectiveness of the control method.

To further improve IAS performance, the cooperative between OMA and IMA was designed. A controller based on MPC theory was designed to compute the best suspension. Simultaneously, the rule is defined to distribute the best suspension force between IMA and OMA. The effectiveness of the proposed cooperative control strategy is examined through simulation and vehicle tests.

The remainder of the paper is organized as follows. In Section 2, the model of the system is introduced. The controller based on MPC theory is designed, and the simulation results are presented in Section 3. The vehicle test results are discussed in Section 4 before the paper is concluded in Section 5.

2. The Modeling of the System

2.1. Interconnected Air Suspension Development

A novel IAS, which is introduced in this paper, consists of OMA and four-corner IMA. IAS configuration is shown in Figure 1.

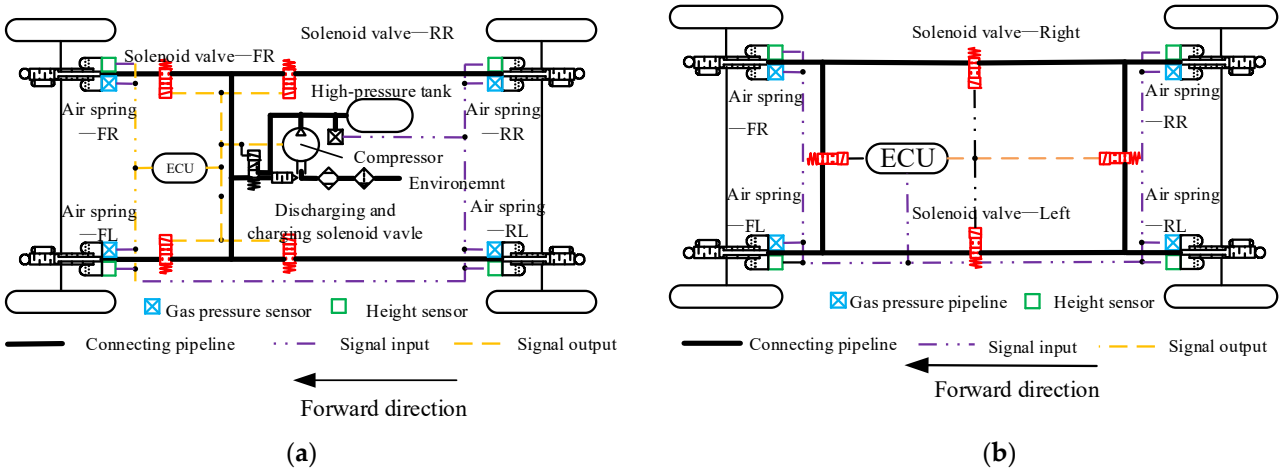

Figure 1. Interconnected air spring system configuration. (**a**) The configuration and working principle of outsourced mode activation. (**b**) The configuration and working principle of interconnected mode activation.

In Figure 1a, the OMA is composed of pipelines of a charging and discharging solenoid valve, compressor, and high-pressure tank. The ECU controls working duration of the OMA by opening or closing the solenoid valves for charging and discharging.

In Figure 1b, the IMA is composed of four air springs, four solenoid valves, and interconnected pipelines. The ECU changes the interconnection mode of the ISA by opening or closing the solenoid valves in the pipeline. When all solenoid valves are closed, air suspension is non-interconnected; when all solenoid valves are opened, air suspension is four-corner-interconnected; when the solenoid valve-Front and solenoid valve-Rear are opened and solenoid valve-Left solenoid valve and solenoid valve-Right are closed, air suspension is lateral interconnected; when solenoid valve-Left and solenoid valve-Right are open and solenoid valved-Front and solenoid valve-Rear are closed, air spring is longitudinal interconnected.

2.2. Full-Vehicle Vertical Model

The vehicle is modeled based on the moving vehicle coordinate system, *XYZ*, which is attached at the center of gravity (CG) and aligned in principal directions. The full-vehicle vehicle model is simplified to seven degrees of freedom (7-DOF): vertical motions of four wheels, the roll motion, pitch motion, and vertical motion of sprung mass. The 7-DOF structure of the full-vehicle physical model shown in Figure 2 has been verified by testing [6].

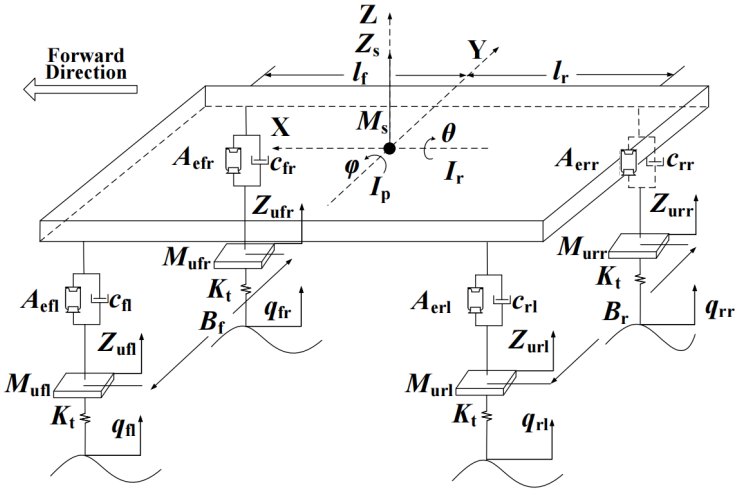

Figure 2. Seven-degree-of-freedom physical model of the full vehicle.

Here, M_s is the sprung mass; Z_s is vertical displacement at the center of gravity; I_r and I_p denote roll and pitch moments of inertia, respectively; θ and φ are the roll angle and pitch angle of the vehicle body, respectively; l_f and l_r are the distances between the center of gravity to the front and the rear axis; B_f and B_r are treads of front and rear wheels, respectively; the front and rear unsprung masses on the right and left sides, respectively, are denoted by M_{ufl}, M_{ufr}, M_{url}, and M_{urr}; Z_{ufl}, Z_{ufr}, Z_{url}, and Z_{urr} are the vertical displacements of the four wheels; K_t denotes the tire stiffness of the wheels; q_{fl}, q_{fr}, q_{rl} and q_{rr} are road roughness displacements; A_{efl}, A_{efr}, A_{erl}, and A_{err} are effective areas of four air suspensions; c_{ufl}, c_{ufr}, c_{url}, and c_{urr} are the damping coefficients of four suspensions.

Thus, the 7-DOF model of the full-vehicle dynamic model is written as follows

$$\begin{cases} M_s\ddot{Z}_s = F_{fl} + F_{fr} + F_{rl} + F_{rr} \\ I_r\ddot{\theta} = (F_{fl} - F_{fr})\frac{B_f}{2} + (F_{rl} - F_{rr})\frac{B_r}{2} \\ I_p\ddot{\varphi} = (F_{fl} + F_{fr})l_f - (F_{rl} + F_{rr})l_r \\ M_{ufl}\ddot{Z}_{ufl} = K_t(Z_{tfl} - q_{fl}) - F_{fl} \\ M_{ufr}\ddot{Z}_{ufr} = K_t(Z_{tfr} - q_{fr}) - F_{fr} \\ M_{url}\ddot{Z}_l = K_t(Z_{trl} - q_{rl}) - F_{rl} \\ M_{urr}\ddot{Z}_{urr} = K_t(Z_{trr} - q_{rr}) - F_{rr} \end{cases} \quad (1)$$

in which

$$\begin{cases} fd_{\mathrm{fl}} = Z_{\mathrm{s}} - Z_{\mathrm{ufl}} - l_{\mathrm{f}}\varphi + 0.5\theta B_{\mathrm{f}} \\ fd_{\mathrm{fr}} = Z_{\mathrm{s}} - Z_{\mathrm{ufr}} - l_{\mathrm{f}}\varphi - 0.5\theta B_{\mathrm{f}} \\ fd_{\mathrm{rl}} = Z_{\mathrm{s}} - Z_{\mathrm{url}} + l_{\mathrm{r}}\varphi + 0.5\theta B_{\mathrm{r}} \\ fd_{\mathrm{rr}} = Z_{\mathrm{s}} - Z_{\mathrm{urr}} + l_{\mathrm{r}}\varphi - 0.5\theta B_{\mathrm{r}} \end{cases} \tag{2}$$

where, fd_{fl}, fd_{fr}, fd_{rl}, and fd_{rr} are the suspension dynamic travels of the four suspensions. F_{fl}, F_{fr}, F_{rl}, and F_{rr} are suspension forces which consist of damping force and air suspension force.

The parameters of these equations are listed in Table 1.

Table 1. Parameters of the vehicle model.

Parameter	Value	Parameter	Value
M_{s} (kg)	4500	l_{r} (mm)	1270
M_{ufl}, M_{ufr} (kg)	300	K_{t} (kN/m)	210
M_{url}, M_{urr} (kg)	500	B_{f} (mm)	1665
I_{r} (kg·m^2)	3757	B_{r} (mm)	1525
I_{p} (kg·m^2)	7391	c_{ufl}, c_{ufr}, c_{url}, c_{urr} (N·s/m)	2600
l_{f} (mm)	2665	A_{efl}, A_{efr}, A_{erl}, A_{err} (m^2)	0.03

3. Cooperative Control Design Based on MPC

3.1. MPC Controller Design

There are outstanding advantages, applying MPC theory, in dealing with the optimization problem with constraints in a finite time domain, so it has numerous applications in the field of suspension control [13]. The MPC controller flow chart of the whole control system is shown in Figure 3. In Figure 3, a cooperative control strategy using MPC theory is designed based on the linear full-vehicle vertical model to compute the best suspension force. Then, the rule is defined to distribute the best suspension force between IMA and OMA. Finally, the generated suspension force is fed back to the system. $\hat{\boldsymbol{x}}$ is the estimated value of vehicle state variables; $\boldsymbol{y}(t)$ is system output.

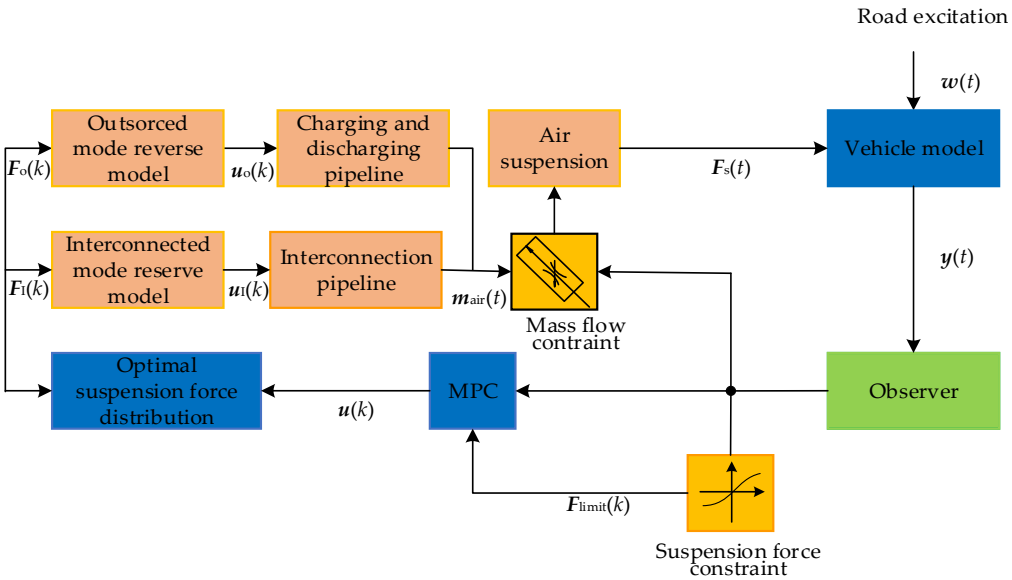

Figure 3. Cooperative control flow chart of interconnected air suspension.

The nonlinear characteristic in the established model makes the controller more complicated and reduces computational efficiency. Thus, it is necessary to linearize to meet the requirements of the high real-time application scenarios of suspension control. When

the solenoid valves in the OMA and IMA are turned off, the full-vehicle linear state space equation is written as:

$$\begin{cases} \dot{\boldsymbol{x}}(t) = \boldsymbol{A}\boldsymbol{x}(t) + \boldsymbol{B}_{\mathrm{u}}\boldsymbol{u}(t) + \boldsymbol{B}_{\omega}\boldsymbol{\omega}(t) \\ \boldsymbol{y}(t) = \boldsymbol{C}\boldsymbol{x}(t) + \boldsymbol{D}_{\mathrm{u}}\boldsymbol{u}(t) + \boldsymbol{D}_{\omega}\boldsymbol{\omega}(t) \end{cases} \tag{3}$$

The state vector is defined as follows:
$\boldsymbol{x} = [Z_{\mathrm{s}}, \dot{Z}_{\mathrm{s}}, \theta, \dot{\theta}, \varphi, \dot{\varphi}, Z_{\mathrm{ufl}}, \dot{Z}_{\mathrm{ufl}}, Z_{\mathrm{ufr}}, \dot{Z}_{\mathrm{ufr}}, Z_{\mathrm{url}}, \dot{Z}_{\mathrm{url}}, Z_{\mathrm{urr}}, \dot{Z}_{\mathrm{urr}}]^{\mathrm{T}}$
The input vector is defined as follows:
$\boldsymbol{U} = [u_{\mathrm{fl}}, u_{\mathrm{fr}}, F_{\mathrm{rl}}, F_{\mathrm{rr}}]^{\mathrm{T}}$; $\omega = [q_{\mathrm{fl}}, q_{\mathrm{fr}}, q_{\mathrm{rl}}, q_{\mathrm{rr}}]^{\mathrm{T}}$
The output vector is defined as follows:
$\boldsymbol{Y} = [\ddot{Z}_{\mathrm{sfl}}, \ddot{Z}_{\mathrm{sfr}}, \ddot{Z}_{\mathrm{srl}}, \ddot{Z}_{\mathrm{srr}}, \ddot{Z}_{\mathrm{ufl}}, \ddot{Z}_{\mathrm{ufr}}, \ddot{Z}_{\mathrm{url}}, \ddot{Z}_{\mathrm{urr}}, fd_{\mathrm{fl}}, fd_{\mathrm{fr}}, fd_{\mathrm{rl}}, fd_{\mathrm{rr}}]^{T}$.

where u_{fl}, u_{fr}, u_{rl}, and u_{rr} are the suspension control force. $\boldsymbol{A}$, $\boldsymbol{B}_{\mathrm{u}}$, $\boldsymbol{B}$, $\boldsymbol{C}$, $\boldsymbol{D}_{\mathrm{u}}$ are corresponding Jacobian matrices. $\boldsymbol{B}_{\boldsymbol{\omega}}$, $\boldsymbol{D}_{\boldsymbol{\omega}}$ are disturbance matrixes.

When the IMA and OMA work, the pressure change in the air spring is linearized, cited by [19]

$$\begin{cases} \dot{\boldsymbol{P}}_i = \boldsymbol{A}_i\boldsymbol{q}_i \\ \dot{\boldsymbol{q}}_i = \boldsymbol{A}_i\boldsymbol{P} + \boldsymbol{B}_i\boldsymbol{q}_i \end{cases} \tag{4}$$

For IMA, $i = I$, matrix $\dot{\boldsymbol{P}}_{\mathrm{I}} = \left[\dot{P}_{\mathrm{Ifl}},\ \dot{P}_{\mathrm{Ifr}},\ \dot{P}_{\mathrm{Irl}},\ \dot{P}_{\mathrm{Irr}}\right]^{\mathrm{T}}$ represents the pressure change rate of the front-left (FL), front-right (FR), rear-left (RL), and rear-right (RR) air springs due to IMA; matrix $\boldsymbol{P}$ is the current pressure in the FL, FR, RL, and RR air spring; matrix $\dot{\boldsymbol{q}}_{\mathrm{I}} = \left[\dot{q}_{\mathrm{Ifl}},\ \dot{q}_{\mathrm{Ifr}},\ \dot{q}_{\mathrm{Irl}},\ \dot{q}_{\mathrm{Irr}}\right]^{\mathrm{T}}$ represents the total gas mass flow change of the FL, FR, RL, and RR air springs; $\boldsymbol{A}_{\mathrm{pI}}$, $\boldsymbol{B}_{\mathrm{p}}$, $\boldsymbol{A}_{\mathrm{qI}}$, and $\boldsymbol{B}_{\mathrm{qI}}$ are the corresponding state matrixes. In OMA, $i = H$, matrix $\dot{\boldsymbol{P}}_{\mathrm{o}} = \left[\dot{P}_{\mathrm{Hfl}},\ \dot{P}_{\mathrm{Hfr}},\ \dot{P}_{\mathrm{Hrl}},\ \dot{P}_{\mathrm{Hrr}},\ \dot{P}_{\mathrm{t}}\right]^{\mathrm{T}}$ refer to the pressure change rate of FL, FR, RL, and RR air springs and high-pressure tanks; $\boldsymbol{q} = \left[\boldsymbol{P}_{\mathrm{o}} + \boldsymbol{B}_{\mathrm{p}}\boldsymbol{x},\ P_{\mathrm{t}},\ \mathrm{P_a}\right]^{\mathrm{T}}$ are the current pressure of air springs, high-pressure tank pressure, and atmospheric pressure, respectively.

The existing continuous-time state equation is discretized by the sample time T_{s} and the zero-order holder considering MPC used to solve the optimization problem in the discrete-time domain. The discretized equation of state is described as

$$\begin{cases} \boldsymbol{x}[k+1] = \boldsymbol{A}_{\mathrm{d}}\boldsymbol{x}[k] + \boldsymbol{B}_{\mathrm{du}}\boldsymbol{u}[k] + \boldsymbol{B}_{\mathrm{d}\omega}\boldsymbol{\omega}[k] \\ \boldsymbol{y}[k] = \boldsymbol{C}_{\mathrm{d}}\boldsymbol{x}[k] + \boldsymbol{D}_{\mathrm{du}}\boldsymbol{u}[k] + \boldsymbol{D}_{\mathrm{d}\omega}\boldsymbol{\omega}[k] \end{cases} \tag{5}$$

in which

$$\boldsymbol{A}_{\mathrm{d}} = e^{\boldsymbol{A}T_s} = \mathcal{L}^{-1}\left\{(s\mathbf{I} - \boldsymbol{A})^{-1}\right\}_{\mathrm{t=T_s}}$$

$$\begin{bmatrix} \boldsymbol{B}_{\mathrm{du}} \\ \boldsymbol{B}_{\mathrm{d}\omega} \end{bmatrix} = \left(\int_{\tau=0}^{T_{\mathrm{s}}} e^{\boldsymbol{A}\tau}d\tau\right)\begin{bmatrix} \boldsymbol{B}_{\mathrm{u}} \\ \boldsymbol{B}_{\omega} \end{bmatrix} = \boldsymbol{A}^{-1}(\boldsymbol{A}_{\mathrm{d}} - I)\begin{bmatrix} \boldsymbol{B}_{\mathrm{u}} \\ \boldsymbol{B}_{\omega} \end{bmatrix}$$

$$\boldsymbol{C}_{\mathrm{d}} = \boldsymbol{C}$$

$$\boldsymbol{D}_{\mathrm{d}} = \boldsymbol{D}$$

The standard form of MPC controller cost function is obtained as

$$J = \sum_{i=1}^{N}\Big(y(k+i) - y_{ref}(k+i)\Big)^{T} Q_i\Big(y(k+i) - y_{ref}(k+i)\Big) + \sum_{0}^{N-1} u(k+i)^{T} P_i(u(k+i)) \tag{6}$$

in which $\boldsymbol{Q}_i$ and $\boldsymbol{R}_i$are symmetric and positive definite weighting matrices. Matrix $\boldsymbol{Q}_i$ is chosen to minimize sprung mass vertical acceleration of the vehicle $\left[\ddot{Z}_{\mathrm{sfl}}, \ddot{Z}_{\mathrm{sfr}}, \ddot{Z}_{\mathrm{srl}}, \ddot{Z}_{\mathrm{srr}}\right]$, the suspension dynamic travels $[Z_{\mathrm{sfl}} - Z_{\mathrm{ufl}}, Z_{\mathrm{sfr}} - Z_{\mathrm{ufr}}, Z_{\mathrm{srl}} - Z_{\mathrm{url}}, Z_{\mathrm{srr}} - Z_{\mathrm{urr}}]$, and the vertical displacements of the four tires $[Z_{\mathrm{ufl}} - q_{\mathrm{fl}}, Z_{\mathrm{ufr}} - q_{\mathrm{fr}}, Z_{\mathrm{url}} - q_{\mathrm{rl}}, Z_{\mathrm{urr}} - q_{\mathrm{rr}}]$; matrix Ri is the weight of demanded energy; $\boldsymbol{y}_{\mathrm{ref}}$ is the reference signal.

In the real system, suspension dynamic travels and suspension control forces $\boldsymbol{u}$, which are generated by IMA and OMA, are limited by physical restrictions. These constraints in MPC controller ensure that the optimal control quantity is within the range of suspension capacity.

The suspension control force of four air springs $U_{\mathrm{I}i}$ in IMA are constrained as

$$\begin{cases} 0 \le U_{\mathrm{I}i} \le \Delta P_{\mathrm{I}i}[k] A_{\mathrm{e}i} & q_{\mathrm{i}}[k] \ge 0 \\ \Delta P_{\mathrm{I}i}[k] A_{\mathrm{e}i} \le U_{\mathrm{I}i} \le 0 & q_i[k] < 0 \end{cases} \tag{7}$$

where $\Delta P_{\mathrm{I}i}[k]$ (i = fl, fr, rl, rr) are air pressure change values generated by IMA in k sampling time; $q_i[k]$ (i = fl, fr, rl, rr) are air mass flows of air springs in k sampling time.

Moreover, this is expressed as a standard form:

$$\begin{cases} \boldsymbol{R}_{\mathrm{I}} \boldsymbol{u}_{\mathrm{I}} \le \boldsymbol{C}_{\mathrm{Ic1}}(\boldsymbol{x}) & \boldsymbol{C}_{\mathrm{Is}} \boldsymbol{k} \le 0 \\ \boldsymbol{R}_{\mathrm{I}} \boldsymbol{u}_{\mathrm{I}} \le \boldsymbol{C}_{\mathrm{Ic2}}(\boldsymbol{x}) & \boldsymbol{C}_{\mathrm{Is}} \boldsymbol{k} > 0 \end{cases} \tag{8}$$

The suspension control forces of four air springs $U_{\mathrm{o}i}$ in OMAs are constrained as

$$\Delta P_{\mathrm{d}i}[k] A_{\mathrm{e}i} \le U_{\mathrm{o}i} \le \Delta P_{ci}[k] A_{\mathrm{e}i} \tag{9}$$

in which $\Delta P_{\mathrm{o}i}[k]$ (i = fl, fr, rl, rr) represent four air spring pressure change values changed by OMA.

Equation (9) is transformed into the matrix form similarly.

$$\boldsymbol{R}_{\mathrm{o}} \boldsymbol{u}_{\mathrm{o}} \le \boldsymbol{C}_{\mathrm{oc}}(\boldsymbol{u}) \tag{10}$$

Combining the above-mentioned suspension control force constraint, the constraint of the full-vehicle control quantity $\boldsymbol{u}$ is expressed as their intersection. The constraints of suspension dynamic travel are set as

$$f d_i^{\mathrm{down}} \le f d_i \le f d_i^{\mathrm{up}} \tag{11}$$

where $f d_i^{\mathrm{down}}$ are suspension compression travel limits; $f d_i^{\mathrm{up}}$ are suspension stretch travel limits.

The constraints of suspension dynamic travel are described by matrix forms:

$$\boldsymbol{C}_{\mathrm{x}} \boldsymbol{\gamma} \le \boldsymbol{b} \tag{12}$$

Finally, the optimization problem is described as

$$\begin{gathered} \min_{u}(J) \\ \text{s.t.} \\ \boldsymbol{x}_{\mathrm{k+1}} = \boldsymbol{A}_{\mathrm{d}} \boldsymbol{x}_{\mathrm{k}} + \boldsymbol{B}_{\mathrm{du}} \boldsymbol{u}_{\mathrm{k}} + \boldsymbol{B}_{\mathrm{d}\omega} \boldsymbol{\omega}_{\mathrm{k}} \\ \boldsymbol{C}_{\mathrm{x}} \boldsymbol{\gamma} \le \boldsymbol{b} \\ \boldsymbol{u} \in \boldsymbol{U},\ \boldsymbol{U} = (8) \wedge (10) \end{gathered} \tag{13}$$

This optimization problem is transformed into a QP (Quadratic Program) problem and is solved by the most typical methods such as the positive set method and interior point method.

3.2. Rule of Best Suspension Force Distribution for IMA and OMA

Although the effect of the equivalent suspension force generated by IMA and OMA on the full-vehicle systems is the same, the consumption of the equivalent suspension force

generated by them is completely different. The objective of this section is to minimize the action cost and energy consumption of the control system.

As the power of the interconnected solenoid valve is set as E_{I} W, the action cost of the IMA in each sampling interval is set as

$$J_I(t_{Ii}) = \sum_{i=1}^{4} \int_0^{t_i} E_I dt = E_I \sum_{i=1}^{4} t_{Ii} \tag{14}$$

where t_{Ii} (i = fl, fr, rl, rr) represents the solenoid valves' operating time in the four interconnected pipelines.

In the sampling interval, the total action cost of the OMA is expressed as

$$J_{\mathrm{o}}(t_{\mathrm{ci}}, t_{\mathrm{di}}) = J_{\mathrm{ov}}(t_{\mathrm{ci}}, t_{\mathrm{di}}) + J_{\mathrm{oa}}(t_{\mathrm{ci}}, t_{\mathrm{di}}) \tag{15}$$

in which J_{ov} refers to the energy consumption of the charging and discharging solenoid valves. J_{oa} relates to the cost of the OMA used to alter the gas quality in the air spring during charging and discharging.

The power of the charging and discharge solenoid valve is set as E_{o}W, and the action cost of the OMA during each sampling interval is

$$J_{\mathrm{ov}}(t_{ci}, t_{di}) = \sum_{i=1}^{4} \left(\int_0^{t_{\mathrm{ci}}} E_{\mathrm{o}} dt + \int_0^{t_{di}} E_{\mathrm{o}} dt \right) = E_{\mathrm{o}} \cdot \sum_{i=1}^{4} (t_{ci} + t_{di}) \tag{16}$$

There is no possibility of charging and discharging simultaneously.

$$t_{\mathrm{ci}} \cdot t_{\mathrm{di}} = 0 \tag{17}$$

During the charging process, in addition to the energy consumed by the charging and discharging solenoid valves, the gas filled into the air spring is compressed by an air compressor into the high-pressure tank. The air compressor supplements the high-pressure tank with the same quality of gas through the atmosphere when OMA fills the air spring with a certain quality of gas, shown as follows:

$$J_{\mathrm{Oa}}(t_{ci}, t_{di}) = \sum_{i=1}^{4} \{K_{\mathrm{c}} \cdot q_{ci}[k] \cdot t_{\mathrm{ci}} + K_{\mathrm{d}} \cdot q_{di}[k] \cdot t_{\mathrm{d}i}\} \tag{18}$$

As cited in [6], K_{c} and K_{d} are coefficients.

The energy consumption cost of the control system is

$$J_{\mathrm{E}} = J_{\mathrm{I}} + J_{\mathrm{o}} \tag{19}$$

In the case of a minimal sampling interval, the system is regarded as quasi-static within the sampling interval. Regardless of the controllable structure that provides the best suspension force, the effect of suspension force on the whole vehicle system remains constant. Thus, the change in energy consumption cost with the force generated by each agent is a monotonically increasing function. On the basis of the above assumptions, a best suspension force distribution method is proposed.

$$\Delta J_i = G_i(F, \Delta F) \tag{20}$$

In order to reduce the internal air pressure difference for each air spring, it is necessary to further divide the responsibilities of IMA and OMA.

In case the target can be approached through IMA, it can be divided into three categories. Three categories of pressure in the air suspension are shown in Table 2.

Table 2. Three categories of pressure in the air suspension.

Number	Case
1	The target pressure cannot be achieved.
2	The low-pressure air spring reaches the target pressure first, while the high-pressure air spring must continue discharging to reach the target pressure.
3	The air spring on the high-pressure side reaches the target air pressure first, while the air spring on the low-pressure side needs to inflate further to reach the target air pressure.

For the two cases of 2 and 3, the IMA should be stopped and needs further discussion when one side reaches the target pressure. In the case of situation 2, if the air spring on the low-pressure side reaches the target pressure, the IMA will be immediately stopped. The OMA must discharge gas the air spring at the high-pressure side. Obviously, the energy consumption cost of the OMA is increased. In this case, the energy consumption cost of the air spring at the high-pressure side discharge to the target air pressure is set as J_{H0d}, according to the current cost of bleeding the air spring on the high-pressure side to achieve the target air pressure. If the pressure balance interconnection on two sides of the interconnection pipeline is closed when the air spring on the low-pressure side reaches the target air pressure, it follows that the low-pressure air spring must be deflated by the OMA to achieve the target air pressure. Moreover, the air spring on the high-pressure side may be charged and discharged by OMA. The energy consumption of adjusting the air spring pressure at the high-pressure and low-pressure sides to the target pressure are set as J_{Hd} and J_{Ld}, respectively. This is due to the time required for IMA. At this point, the problem becomes comparing the size of J_{H0d} and $J_{Hd} + J_{Ld}$.

In the above discussion, the initial state and the end state of the two interconnected air springs are fixed. In other words, in case 2, IMA composed of two air springs must discharge a certain amount of gas to ensure a terminal state. It has nothing to do with the process, therefore $J_{H0d} = J_{Hd} + J_{Ld}$. However, since the continued IMA consumes a certain amount of energy, as soon as the air spring on the low-pressure side reaches the target pressure in case 2, the IMA shall be immediately disconnected, as in case 3. In Figure 4, we see the selection of actions under different states for the IMA and OMA.

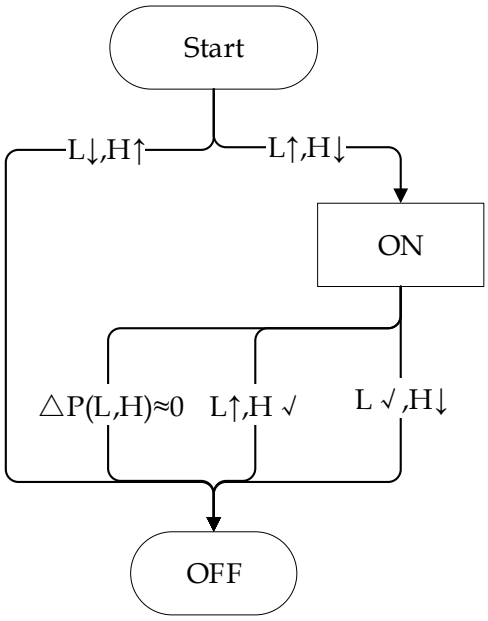

Figure 4. Action of solenoid valves in interconnected mode activation by judging different pressure condition in two-side of interconnected air suspension. In which, Δ*P* (L, H) represents the pressure difference between the high- and low-pressure sides; L represents low-pressure side; H represents high-pressure; ↑ represents increasing pressure; ↓ represents decreasing pressure; √ represents reaching targeted pressure.

The discussion above clarifies the differing responsibilities of IMA and OMA, both of which are capable of modifying air spring pressure. Figure 4 also serves as a constraint for the calculation of energy costs in IMA, if interconnection can be turned on at this time. Afterward, the energy consumption cost can be computed normally; if the interconnection should be closed at this time, the energy consumption cost is set to positive infinity. Accordingly, if suspension control force $\boldsymbol{u}$ is discretized into k parts, the energy consumption costs of the OMA and the IMA control are expressed as follows:

$$J_i^k = G_i\left(F_{opt}^k\right) \tag{21}$$

It is evident that the control unit that consumes the least energy is selected to generate this portion of suspension force, namely,

$$i^{*k} = \min_i J_i^k \tag{22}$$

The control unit corresponding to the best suspension of each part can be obtained from Equation (23) when k gradually increases from 1 to n. Accordingly, the force generated for each control system is

$$F_{si} = \sum_{k=1}^{n} F_{si}^k \tag{23}$$

in which

$$F_{si}^k = \begin{cases} F_{\text{opt}}^k & i = i^* \\ 0 & i \neq i^* \end{cases} \tag{24}$$

The specific calculation process for an optimal distribution of suspension force increment with optimal energy consumption is shown in Algorithm 1. In other words, the nonlinear optimization with constraints is simplified to N times energy consumption cost calculation, comparison, and summation calculation through discretization, which not only reduces the calculation effort, but also ensures the lowest energy consumption costs under certain conditions. Normally, as N increases, the more accurate the distribution of force produced by the control system will be obtained, but at the same time, the amount of calculation will also increase proportionately.

Algorithm 1. Procedure for best suspension force distribution with minimal energy consumption.

1. **Initialize** $\boldsymbol{F}_i = 0$
2. **For** $k \leftarrow 1$ **to** n **do**
3. **If** $\forall J_i^k \neq \infty \forall J_i^k \neq \infty$
4. $i^* = \min_i J_i^k$
5. $F_{si^*} = F_{si^*} + F_{\text{opt}}^k$

Return F_{I}, F_{O}

4. Simulation Analysis

MATLAB/Simulink is usually used to simulate the designed controller. The simulation is conducted under the case of C-level and a driving velocity of 20 m/s to examine the effectiveness of the control algorithm. In this simulation, the suspension dynamic travels are set as $\pm$60 mm. Furthermore, the predict step size is set as 30, the control step size is set as 10, and the sampling time T_{s} is 0.01 s. To test the advantages of the proposed cooperative control strategy, the traditional controller is introduced for comparison. In the traditional controller, PID-PWM control strategy and imitated skyhook control strategy [20] are adopted, respectively, in the OMAs and IMAs. The model of imitated sky-hook inter-

connected mode control is shown in Figure 5. The rule of imitating sky-hook interconnected mode control is degenerated into [20]:

$$\text{Interconnecting state} = \begin{cases} \text{Off} & \tau(\tau - \tau_t) > 0 \\ \text{On} & \tau(\tau - \tau_t) \leq 0 \end{cases} \tag{25}$$

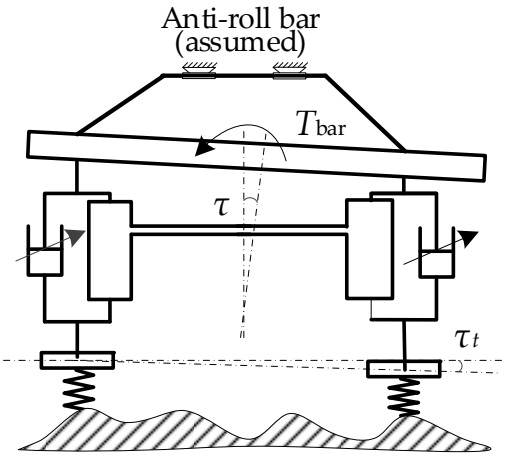

Figure 5. The model of imitated sky-hook interconnected mode control.

In the current sampling time of vehicle state, the suspension forces generated by the OMAs and the IMAs are computed, respectively, combining with the above best suspension force and the method which computes activation actions in Section 3.

The states of interconnected mode activation are illustrated in Figure 6. Pressure changes caused by interconnected mode activation in four air suspensions are shown in Figure 6a, best suspension forces generated by interconnected mode activation are illustrated in Figure 6b and solenoid valve actions in interconnected mode activation are shown in Figure 6c.

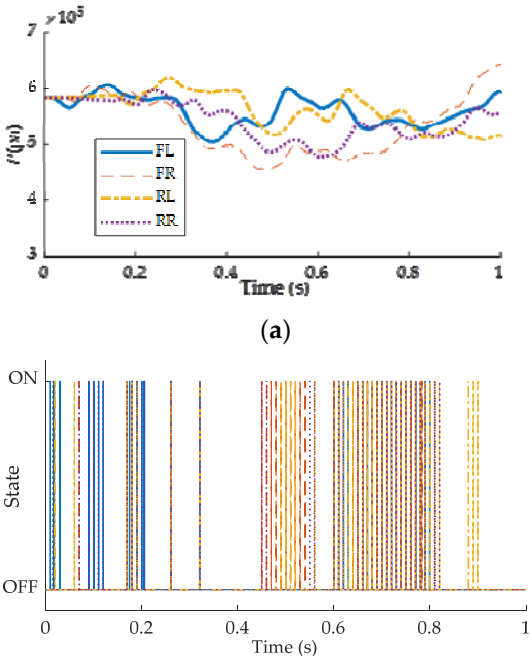

Figure 6. Interconnected mode activation state. (**a**) Pressure changes caused by IMA in four air suspensions. (**b**) Best suspension force generated by IMA. (**c**) Solenoid valve actions in IMA.

As shown in Figure 6a,b, pressure changes and best suspension caused by interconnected mode activation in four air suspensions has relevance. When the force of one air spring decreases due to interconnection, the spring force of one air spring connected with it must increase. Figure 6c shows that the solenoid valves which were acted upon by cooperative controller works.

The states of outsourced mode activation are illustrated in Figure 7. Solenoid valve actions during inflation in outsourced mode activation are shown in Figure 7a, solenoid valve actions during deflation in outsourced mode activation are illustrated in Figure 7b, and best suspension forces generated by outsourced mode activation are shown in Figure 7c.

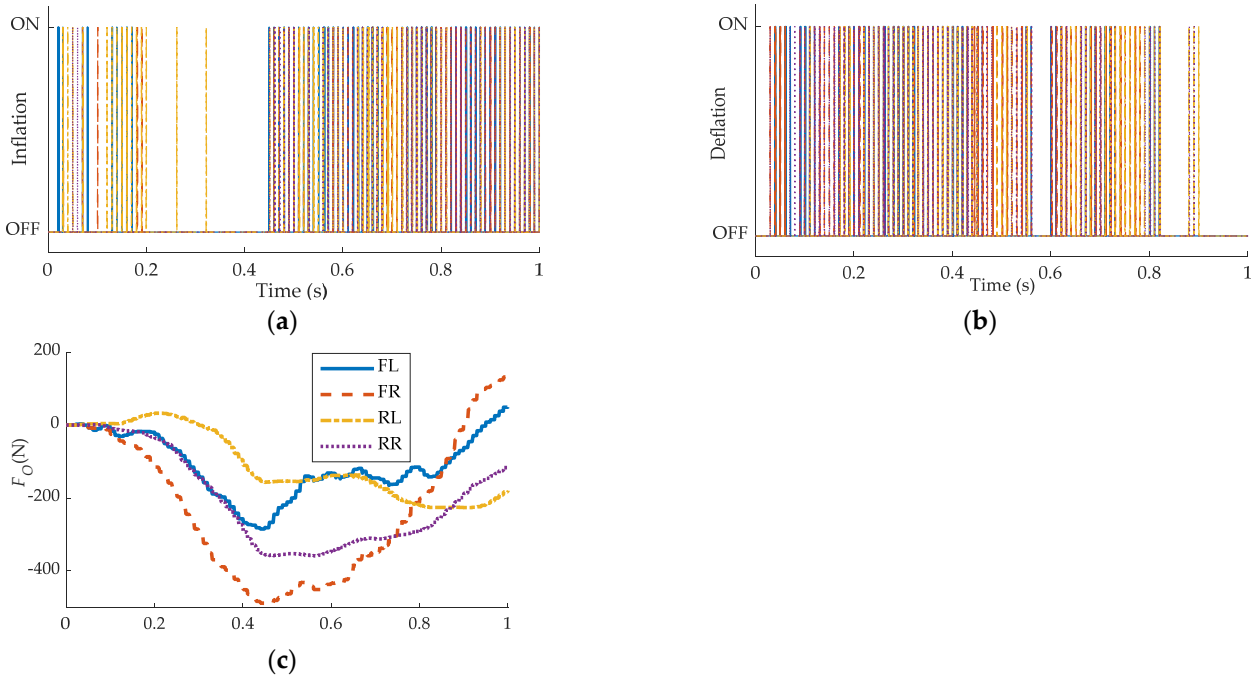

Figure 7. Outsourced mode activation state. (**a**) Solenoid valve actions during inflation in OMA. (**b**) Solenoid valve actions during deflation in OMA. (**c**) Best suspension forces generated by OMA.

As shown in Figure 7a,b, solenoid valve actions during inflation and deflation in outsourced mode activation works well. Figure 7c shows that the best suspension caused by outsourced mode activation has no relevance because the outsourced mode connects to the atmosphere. It not only deflates but also inflates due to the forces have no relevance.

It has been verified in Figures 6 and 7 that the proposed cooperative works effectively. To test ride comfort performance in the full-vehicle, simulation cases were designed ranged from A-level to E-level road in velocities of 30 m/s, respectively.

The performances of cooperative control and traditional control in different cases are shown in Figure 8.

Vehicle ride comfort is a significant index to evaluate vehicle performance [21]. The evaluation indices the root-mean-square value of the sprung mass acceleration (RMS_{Ams}) and root-mean-square value of the tire dynamic (RMS_{fmu}) are chosen to represent vehicle ride comfort. It is known that a lower value indicates better performance [21]. As shown in Figure 8a, RMS_{Ams} reduced 21.18% under E-level road and at most 76.04% under A-level road. RMS_{fmu} reduced 13.18% under E-level road and at most 65.73% under A-level road, as shown in Figure 8b. It is concluded that proposed cooperative control has higher improvement of performance in the better road condition in Figure 8c. The reason is that the best suspension output in the cooperative controller increases with the increase in road excitation amplitude. It is possible that OMA and IMA cannot generate the maximum suspension force required by the controller due to the error of linear model. Therefore, the

improvement reduced under the higher-level road. At the other side, the performance being improved in all working condition indicates that the constraints set in the MPC works.

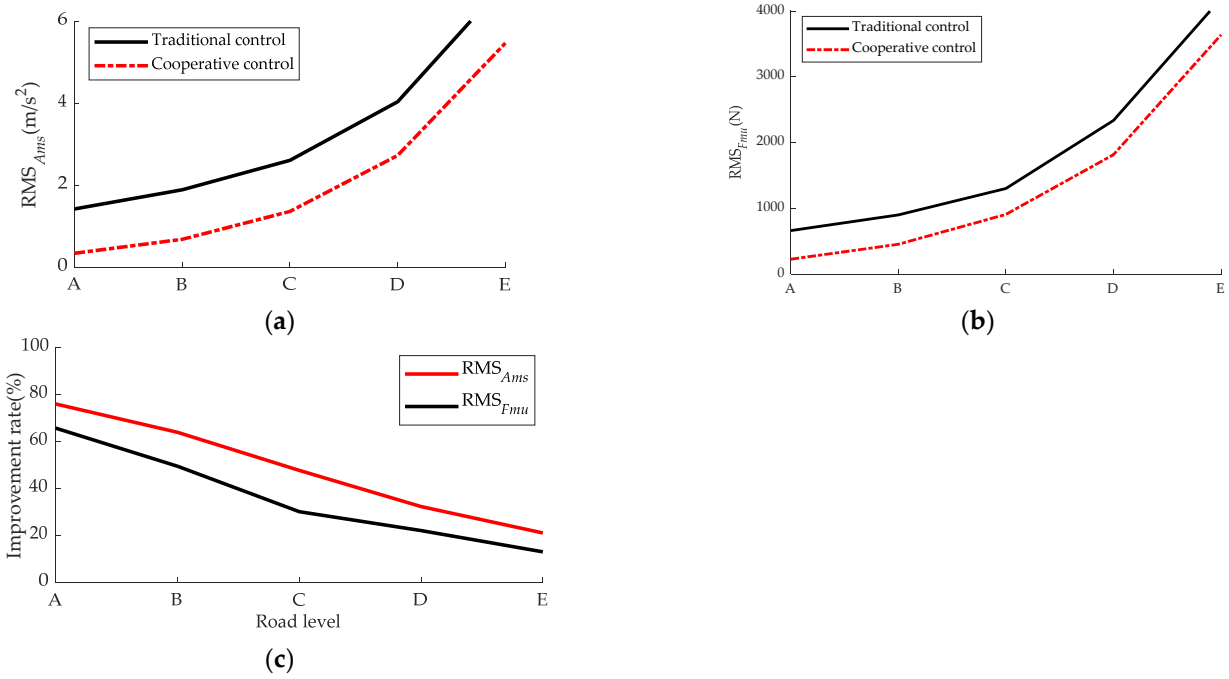

Figure 8. Performance comparisons between traditional and cooperative control at 30 m·s^{-1}. (**a**) Comparison of RMS$_{Ams}$ between traditional control and cooperative control. (**b**) Comparison of RMS$_{fmu}$ between traditional control and cooperative control. (**c**) Improvement rate of RMS$_{Ams}$ and RMS$_{fmu}$ under different road level.

5. Vehicle Test

To examine the proposed cooperative control strategy, experiments are performed with a test vehicle shown in Figure 9. The test vehicle is a medium-sized bus produced by Nanjing Golden Dragon Bus Co., Ltd. (Nanjing, China). The specification of acceleration sensor is shown in Table 3. The sprung mass acceleration sensors are installed near the upper cover plates of the four air springs, respectively, and unsprung mass acceleration sensors are set at the lower cover plates of the four air springs, respectively. In the MPC controller solution process, the controller requires the values of all state variables of the current system to make predictions. In this paper, a Kalman observer cited by [22] is designed to estimate the state variables of the system. Raspberry Pi (RPi) 3B+ is used as the controller hardware of the vehicle test, which is connected to MATLAB/Simulink through the hardware support package. The designed cooperative control designed in Section 3 is stored in MATLAB/Simulink. The signal of sensors uploads to computer for saving in real-time. The test procedure follows the national test standard in China [23] and the velocity is 30 km/h.

The sprung mass acceleration and unsprung mass acceleration of cooperative and traditional control under straight working condition are illustrated in Figure 10. As illustrated in Figure 10, the RMS of the sprung mass vertical acceleration of cooperative control reduced by 24.2% compared with the traditional control (0.4661 m/s^2 and 0.7086 m/s^2, respectively). The RMS of the unsprung mass vertical acceleration reduced by 14.5% (1.8928 m/s^2 and 2.2127 m/s^2, respectively).

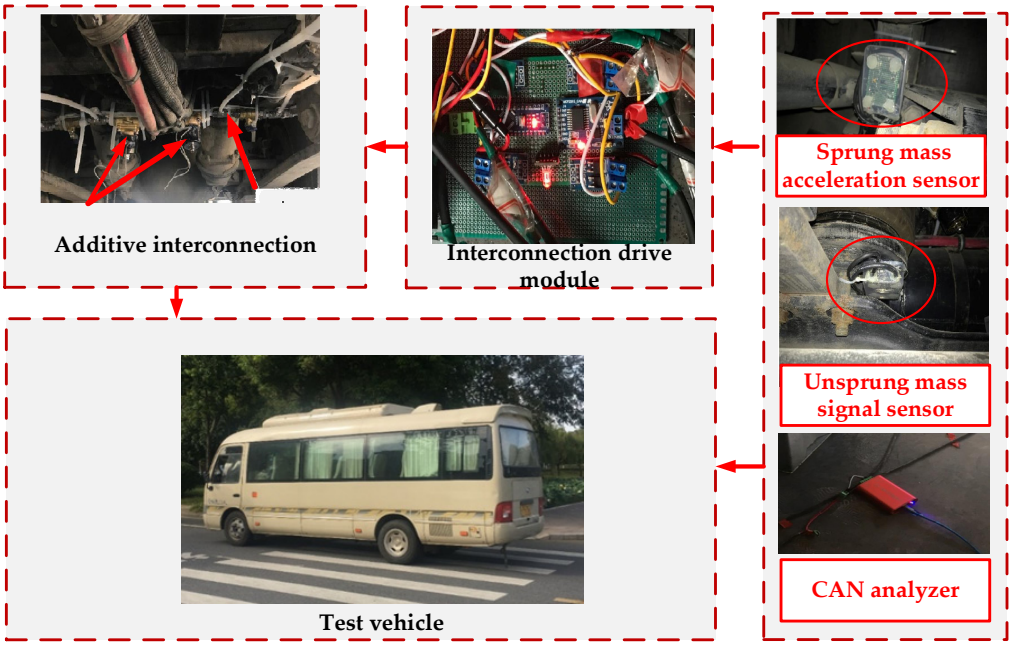

Figure 9. Schematic diagram of the test system.

Table 3. Specification of acceleration sensor.

Specification	Value
Product type	MMA8451Q
Working voltage	1.95 v~3.6 v
Output frequency	1.65~800 Hz
Maximum operating temperature	+85C
Protocol	I^2C

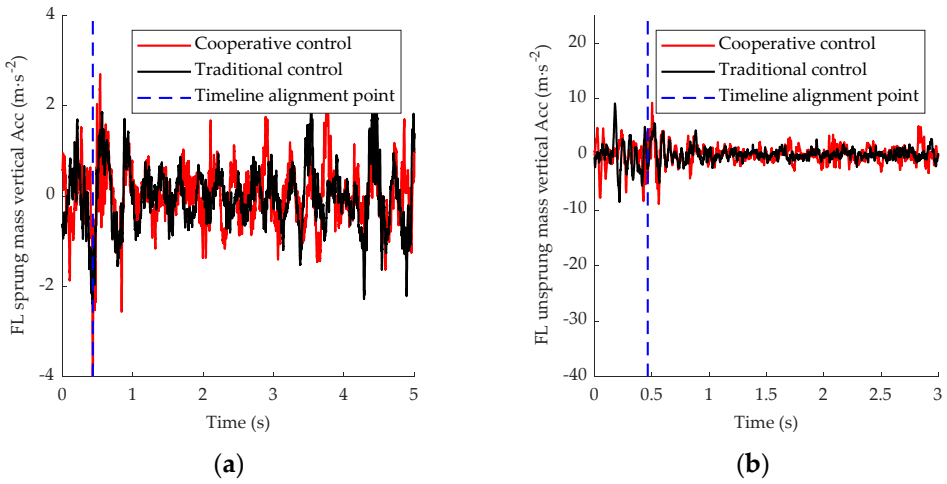

Figure 10. Comparison of cooperative control and traditional control under straight condition. (**a**) Front-left sprung mass vertical acceleration. (**b**) Front-left unsprung mass vertical acceleration.

The sprung mass acceleration and unsprung mass acceleration of cooperative and traditional control under bump working condition are illustrated in Figure 11.

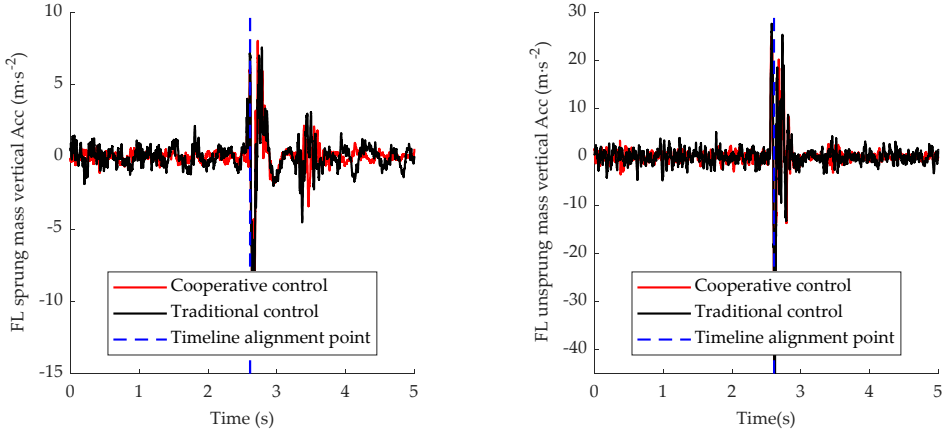

(**a**) (**b**)

Figure 11. Comparison of cooperative and traditional control under bump condition. (**a**) Front-left sprung mass vertical acceleration. (**b**) Front-left unsprung mass vertical acceleration.

As shown in Figure 11, the RMS of the sprung (unsprung) mass acceleration are 1.1694 m/s^2 (3.9133 m/s^2) and 1.4311 m/s^2 (4.6275 m/s^2), respectively, in the cooperative controller and non-cooperative controller. These indexes reduced by 22.38% and 15.43%, respectively.

6. Conclusions

To improve ride comfort in a bus with interconnected air suspension by a minimal energy cost, this paper focuses on cooperative control considering energy consumption between OMA and IMA. Both simulated and experimental results show that proposed cooperative control strategies can significantly improve the performance of ride comfort:

1. A model predictive controller is designed to obtain best suspension force. Simultaneously, the rule is defined to distribute the best suspension force between IMA and OMA.
2. The simulation results show that the indexes of ride comfort including sprung mass acceleration and tire dynamic load in the cooperative controller are significantly improved compared with non-cooperative controller under different road levels.
3. The vehicle on-road test verified that the designed cooperative controller improved the ride comfort, especially, the RMS of the sprung mass acceleration of cooperative control reduced by 24.2% compared with the traditional control (0.4661 m/s^2 and 0.7086 m/s^2, respectively), and the RMS of the unsprung mass acceleration reduced by 14.5% (1.8928 m/s^2 and 2.2127 m/s^2, respectively) under the straight working condition. Under the bump condition, the RMS of the sprung (unsprung) mass acceleration are 1.1694 m/s^2 (3.9133 m/s^2) and 1.4311 m/s^2 (4.6275 m/s^2), respectively, in the cooperative controller and traditional controller. The indexes reduced by 22.38% and 15.43%, respectively. The experimental results show that the proposed control strategy not only makes the IMA and OMA work effectively, but also the ride comfort under different working conditions has significantly improved.

The simulation and vehicle on-road test results show that the proposed cooperative control is feasible. Therefore, it is believed that the proposed cooperative control has a wonderful application in the bus to improve vehicle ride comfort. In following works, the cooperative control used in controllable structures will be explored further.

Author Contributions: Funding acquisition, Z.L.; Methodology, W.Y.; Project administration, Y.Y.; Software, Y.Z.; Validation, W.Y.; Writing—original draft, Y.Z.; Writing—review and editing, Y.Z. All authors have read and agreed to the published version of the manuscript.

Funding: This work was supported by National Natural Science Foundation of China (grant number 51975254).

Institutional Review Board Statement: Not applicable for studies not involving humans or animals.

Informed Consent Statement: Not applicable for studies not involving humans.

Data Availability Statement: The data presented in this study are available on request from the corresponding author. The data are not publicly available due to privacy.

Conflicts of Interest: The authors declare no conflict of interest.

References

1. Li, G.; Ruan, Z.Y.; Gu, R.H.; Hu, G.L. Fuzzy sliding mode control of vehicle magnetorheological semi-active air suspension. *Appl. Sci.* **2021**, *11*, 10925. [CrossRef]
2. Qi, H.M.; Chen, Y.C.; Zhang, N.; Zhang, B.J.; Wang, D.; Tan, B. Improvement of both handling stability and ride comfort of a vehicle via coupled hydraulically interconnected suspension and electronic controlled air spring. *Proc. Inst. Mech. Eng. Part D J. Automob. Proc.* **2020**, *234*, 552–571. [CrossRef]
3. Löcken, F.; Welsch, M. The dynamic characteristic and hysteresis effect of an air spring. *Int. J. Appl. Mech. Eng.* **2015**, *20*, 127–145. [CrossRef]
4. Stone, E.J.; Cebon, D. An experimental semi-active anti-roll system. *Proc. Inst. Mech. Eng. Part D J. Automob. Proc.* **2008**, *222*, 2415–2433. [CrossRef]
5. Kat, C.J.; Els, P.S. Interconnected air spring model. *Math. Comput. Model., Dyn. Syst.* **2009**, *15*, 353–370. [CrossRef]
6. Li, Z.X.; Ju, L.Y.; Jiang, H.; Xu, X.; Li, M. Experimental and simulation study on the vibration isolation and torsion elimination performances of interconnected air suspensions. *Proc. Inst. Mech. Eng. Part D J. Automob. Proc.* **2016**, *230*, 679–691. [CrossRef]
7. Chiang, H.H.; Lee, L.W. Optimized virtual model reference control for ride and handling performance-oriented semiactive suspension systems. *IEEE Trans. Veh. Technol.* **2015**, *64*, 1679–1690. [CrossRef]
8. Gokul, P.S.; Malar, M.K. A contemporary adaptive air suspension using LQR control for passenger vehicles. *ISA Trans.* **2019**, *93*, 244–254.
9. Sun, L.Q.; Lin, Y.; Geng, G.Q.; Li, Z.X.; Jiang, H.B. Research on switching interconnection modes and game control of interconnected air suspension. *Energies* **2019**, *12*, 3218. [CrossRef]
10. Nazemian, H.; Masih-Tehrani, M. Development of an optimized game controller for energy saving in a novel interconnected air suspension system. *Proc. Inst. Mech. Eng. Part D J. Automob. Proc.* **2020**, *234*, 3068–3080. [CrossRef]
11. Cao, K.; Li, Z.Q.; Gu, Y.L.; Zhang, L.Y.; Chen, L.Q. The control design of transverse interconnected electronic control air suspension based on seeker optimization algorithm. *Proc. Inst. Mech. Eng. Part D J. Automob. Proc.* **2021**, *235*, 2200–2211. [CrossRef]
12. Durmaz, B.E.; Kaçmaz, B.; Mutlu, İ.; Söylemez, M.T. Implementation and comparison of LQR-MPC on active suspension system. In Proceedings of the 2017 10th International Conference on Electrical and Electronics Engineering (ELECO), Bursa, Turkey, 30 November 2017.
13. Rodriguez-Guevara, D.; Favela-Contreras, A.; Beltran-Carbajal, F.; Sotelo, D.; Sotelo, C. Active suspension control using an MPC-LQR-LPV controller with attraction sets and quadratic stability conditions. *Mathematics* **2021**, *9*, 2533. [CrossRef]
14. He, H.W.; Han, M.; Liu, W.; Cao, J.F.; Zhou, N. MPC-based longitudinal control strategy considering energy consumption for a dual-motor electric vehicle. *Energy* **2022**, *253*, 124004. [CrossRef]
15. He, P.; Wen, J.; Stojanovic, V.; Liu, F.; Luan, X.L. Finite-time control of discrete-time semi-Markov jump linear systems: A self-triggered MPC approach. *J. Franklin Inst.* **2022**, *359*, 6939–6957. [CrossRef]
16. Nguyen, M.Q.; Canale, M.; Sename, O.; Dugard, L. A Model Predictive Control approach for semi-active suspension control problem of a full car. In Proceedings of the 2016 IEEE 55th conference on decision and control (CDC), Las Vegas, NV, USA, 12–14 December 2016.
17. Hu, Y.; Chen, M.Z.Q.; Hou, Z.S. Multiplexed model predictive control for active vehicle suspensions. *Int. J. Control* **2015**, *88*, 347–363. [CrossRef]
18. Yang, L.; Wang, R.C.; Ding, R.K.; Liu, W.; Zhu, Z.H. Investigation on the dynamic performance of a new semi-active hydro-pneumatic inerter-based suspension system with MPC control strategy. *Mech. Syst. Signal. Processing* **2021**, *154*, 107569. [CrossRef]
19. Zhu, H.J.; Yang, J.; Zhang, Y.Q. Modeling and optimization for pneumatically pitch-interconnected suspensions of a vehicle. *J. Sound Vib.* **2018**, *432*, 290–309. [CrossRef]
20. Li, Z.X.; Ju, L.Y.; Jiang, H.; Xu, X. Imitated skyhook control of a vehicle laterally interconnected air suspension. *Int. J. Veh. Des.* **2017**, *74*, 204–230. [CrossRef]
21. Wu, H.; Zheng, L.; Li, Y.; Zhang, Z.; Yu, Y. Robust control for active suspension of hub-driven electric vehicles subject to in-wheel motor magnetic force oscillation. *Appl. Sci.* **2020**, *10*, 3929. [CrossRef]
22. *ISO 2631-1:1997*; Mechanical Vibration Shock-Evaluation of Human Exposure to Whole-Body Vibration. ISO: Geneva, Switzerland, 1997.
23. Yang, Z.Y.; Yan, Z.D.; Lu, Y.F.; Wang, W.L.; Yu, L.D.; Geng, Y.F. Double DOF strategy for continuous-wave pulse generator based on extended Kalman filter and adaptive linear active disturbance rejection control. *IEEE Trans. Power Electron.* **2022**, *37*, 1382–1393. [CrossRef]